

This is an Open Access document downloaded from ORCA, Cardiff University's institutional repository: <https://orca.cardiff.ac.uk/id/eprint/100521/>

This is the author's version of a work that was submitted to / accepted for publication.

Citation for final published version:

Celorrio, V., Morris, Louis J., Cattelan, M., Fox, N.A. and Fermin, D.J. 2017. Tellurium-doped lanthanum manganite as catalysts for the oxygen reduction reaction. *MRS Communications* 7 (2) , pp. 193-198. 10.1557/mrc.2017.22

Publishers page: <http://dx.doi.org/10.1557/mrc.2017.22>

Please note:

Changes made as a result of publishing processes such as copy-editing, formatting and page numbers may not be reflected in this version. For the definitive version of this publication, please refer to the published source. You are advised to consult the publisher's version if you wish to cite this paper.

This version is being made available in accordance with publisher policies. See <http://orca.cf.ac.uk/policies.html> for usage policies. Copyright and moral rights for publications made available in ORCA are retained by the copyright holders.



# Tellurium-doped lanthanum manganite as catalysts for the oxygen reduction reaction

V. Celorrio, School of Chemistry, University of Bristol, Cantocks Close, Bristol BS8 1TS, UK

L.J. Morris, School of Chemistry, University of Bristol, Cantocks Close, Bristol BS8 1TS, UK; EPSRC Centre for Doctoral Training in Catalysis, School of Chemistry, Cardiff University, Main Building, Park Place, Cardiff CF10 3AT, UK

M. Cattelan, N.A. Fox, and D.J. Fermin, School of Chemistry, University of Bristol, Cantocks Close, Bristol BS8 1TS, UK

Address all correspondence to: D.J. Fermin at david.fermin@bristol.ac.uk

## Abstract

The effect of tellurium (Te) doping on the electrocatalytic activity of  $\text{La}_{1-x}\text{Te}_x\text{MnO}_3$  toward the oxygen reduction reaction is investigated for the first time.  $\text{La}_{1-x}\text{Te}_x\text{MnO}_3$  with  $x$ -values up to 23% were synthesized from a single ionic liquid-based precursor, yielding nanoparticles with mean diameter in the range of 40–68 nm and rhombohedral unit cell. Electrochemical studies were performed on carbon-supported particles in alkaline environment. The composition dependence activity is discussed in terms of surface density of Mn sites and changes in the effective Mn oxidation state.

## Introduction

Oxygen electrocatalysis is one of the key processes limiting the efficiency of energy conversion devices such as fuel cells, electrolyzers, and metal–air batteries.<sup>[1,2]</sup> In particular, the oxygen reduction reaction (ORR) is commonly associated with slow kinetics, requiring high overpotentials, and high catalyst loadings. Current research activities are also focused on the development of non-noble metal electrocatalysis such as transition metal oxides.<sup>[3,4]</sup> A number of studies have shown that Mn-based transition metal oxides are among the most catalytically active for the ORR in alkaline solutions.<sup>[5–8]</sup> However, the parameters determining the reactivity of Mn sites in this complex systems remain a subject of discussion.

In the case of perovskites oxides ( $\text{ABO}_3$ ), the key active site is determined by the B-cation. A multiplicity of parameters have been linked to electrocatalytic activity such as the nature of the A-site,  $d$ -orbital occupancy in the B-site, oxidation state, A-site surface segregation, oxygen vacancies, particle size, and morphology.<sup>[3,4,9,10]</sup> Suntivich et al. proposed that single occupancy of  $e_g$  orbital gives the highest ORR activity,<sup>[5]</sup> which appears to be supported by DFT studies reported by Calle-Vallejo et al.<sup>[9]</sup> However, recent studies by Celorrio et al. showed that the B-site orbital occupancy may change under operational conditions, concluding that Mn-sites are uniquely active as they undergo changes in the oxidation state in the region close to the formal ORR potential.<sup>[11]</sup> This point has also been recognized by other groups.<sup>[12,13]</sup> The orbital occupancy of Mn can be influenced by the cations occupying the A-site, which might lead to tuning the activity of the catalysts.<sup>[7]</sup> Celorrio et al. also demonstrated that increasing the

amount of  $\text{Ca}^{2+}$  in  $\text{La}_{1-x}\text{Ca}_x\text{MnO}_3$  not only increases the Mn oxidation state, but also decreases the average activity.<sup>[7]</sup>

In this study, we investigate tellurium (Te)-doped lanthanum manganite as an ORR catalyst for the first time. The ratio of Te doping is based on the studies by Yang et al., showing that  $\text{La}_{1-x}\text{Te}_x\text{MnO}_{3+\delta}$  lead to high ratio  $\text{Mn}^{2+}/\text{Mn}^{3+}$ .<sup>[14]</sup>  $\text{La}_{1-x}\text{Te}_x\text{MnO}_3$  is synthesized from a versatile ionic liquid precursor, yielding nanoparticles with size ranging between 40 and 68 nm. At a fixed catalyst loading, the overall performance appears to decrease upon Te doping with respect to  $\text{LaMnO}_3$ . However, normalization of the activity by the number density of electroactive Mn sites reveals a significant improvement of the B-site activity upon 10% Te doping of the A-site.

## Experimental

$\text{La}_{1-x}\text{Te}_x\text{MnO}_3$  were synthesized employing an ionic liquid precursor based on the methodology described in previous studies.<sup>[7,11,15]</sup> Firstly, ~9 mL 69%  $\text{HNO}_3$  was added to a glass vial containing  $\text{TeO}_2$  (0.001 mol) and heated to 80 °C under stirring for 3 h, until the  $\text{TeO}_2$  had completely dissolved. The colorless solution was diluted to 10 mL with deionized water to give a 0.1 M solution of  $\text{Te}^{4+}$  in aqueous  $\text{HNO}_3$ . Later, 0.029 g ethylenediaminetetraacetic acid (EDTA) (0.01 mmol, 1:1 molar ratio of metal precursors:EDTA) was added to 1 mL 1-ethyl-3-methylimidazolium acetate stirred at 80 °C. Then, 0.1 M aqueous  $\text{Mn}(\text{NO}_3)_2 \cdot 4\text{H}_2\text{O}$ ,  $\text{La}(\text{NO}_3)_3 \cdot 6\text{H}_2\text{O}$  and the 0.1 M  $\text{Te}^{4+}$  solution in aqueous  $\text{HNO}_3$  were added to the ionic liquid in the appropriate stoichiometric ratio. The total volume of aqueous solution added was 1 mL. Solutions were dehydrated by heating at 80 °C under stirring for 3 h. Following

dehydration, the mixture was transferred to an alumina crucible containing 100 mg microcrystalline cellulose. After 10 min of stirring at  $\sim 80^\circ\text{C}$ , a slightly viscous homogeneous gel was obtained. The crucible was transferred to a furnace, and calcined at  $850^\circ\text{C}$  for 4 h with a temperature ramp rate of  $5^\circ\text{C}/\text{min}$ . This temperature enabled the formation of phase pure  $\text{La}_{1-x}\text{Te}_x\text{MnO}_3$  with  $x$ -values below 25%.

Powder x-ray diffraction (XRD) was carried out on a Bruker D8 Advance using  $\text{Cu K}\alpha$  radiation. Experiments were run between  $10^\circ$  and  $80^\circ$ , using a step size of  $0.02^\circ$ . The XRD patterns were refined by the Rietveld method using the FULLPROF program.<sup>[16,17]</sup> The following parameters were refined: scale factor, background coefficients, zero-point error and positional coordinates. The isotropic thermal factors for all the atoms were fixed to a standard value of  $1 \text{ \AA}^2$ . No cation deficiency was detected in the case of  $\text{LaMnO}_3$ ; thus the occupancy factors were fixed to 1. For  $\text{La}_{1-x}\text{Te}_x\text{MnO}_3$ , the occupancy factors for La and Te were also refined. Scanning electron microscopy (SEM) was carried out on a JEOL SEM 5600LV scanning electron microscope. Transmission electron microscopy (TEM) was carried out on a JEOL JEM-1400Plus instrument.

X-ray photoelectron spectroscopy (XPS) was carried out at the Bristol NanoESCA Facility equipped with an Argus spectrometer working at a base pressure of  $4.0 \times 10^{-11}$  mbar. Core-level photoemission spectra were acquired in grazing incidence, i.e.  $45^\circ$  between the sample surface and the normal of the electron analyzer, with a monochromatic  $\text{Al K}\alpha$  (1486.7 eV), pass energy of 20 eV at room temperature. The binding energy scale was referenced to the carbon C1s photoemission line.

Cyclic voltammetry was carried out in argon saturated 0.1 M KOH solution using a glassy carbon working electrode, graphite counter electrode, and  $\text{Hg}/\text{HgO}$  reference electrode. Linear sweep voltammetry employing a rotating ring-disk electrode (RRDE) were carried out in  $\text{O}_2$ -saturated 0.1 M KOH solution using an ALS rotation controller, and an Ivium compactstat potentiostat. A glassy carbon disk ( $0.126 \text{ cm}^2$ ) and a Pt ring were used in all experiments. Working electrodes were prepared via a two-step drop-casting process. First, an aqueous Vulcan/Nafion suspension was dropped onto the surface of the electrode, followed by an aqueous suspension of the metal oxide nanoparticles. The sample loading on the electrode surface was  $50 \mu\text{g}_{\text{vulcan}}/\text{cm}^2$ ,  $50 \mu\text{g}_{\text{nafion}}/\text{cm}^2$ , and  $250 \mu\text{g}_{\text{oxide}}/\text{cm}^2$ .

## Results and discussion

Figure 1(a) shows the XRD patterns of  $\text{LaMnO}_3$ ,  $\text{La}_{0.90}\text{Te}_{0.10}\text{MnO}_3$ , and  $\text{La}_{0.77}\text{Te}_{0.23}\text{MnO}_3$  as well as the result of the Rietveld refinement employing a rhombohedral lattice with the space group R3-c.  $\text{LaMnO}_3$  and  $\text{La}_{0.90}\text{Te}_{0.10}\text{MnO}_3$  are characterized by high degree of phase purity, whereas  $\text{La}_{0.77}\text{Te}_{0.23}\text{MnO}_3$  exhibit a small peak associated with an unidentified secondary phase. Ionic liquid precursors incorporating higher Te content yield multiple phases, in agreement

with previous studies.<sup>[18]</sup> Structural parameters were obtained by the Rietveld method and can be found in online Table S1 of the Supporting information. The results show a minimum in the unit-cell volume with increasing Te content (changes below 0.2%), while the Mn–O bond length increases by approximately 0.1% in  $\text{La}_{0.77}\text{Te}_{0.23}\text{MnO}_3$ . These changes in structural parameters appear consistent with previous studies.<sup>[19]</sup>

Figure 1(b) shows a representative SEM image of  $\text{LaMnO}_3$ , illustrating the typical porous microstructure of the synthesized materials, while the TEM image in Fig. 1(c) shows the nano-scale dimensions of the particles (SEM and TEM images of the other oxides can be found in online Figs S1 and S2 of the Supporting Information, respectively). Particle size distributions obtained from measuring at least 80 particles can be found in online Fig. S3, revealing a slight increase in mean particle size with increasing Te content, from  $39.9 \pm 11.3 \text{ nm}$  for  $\text{LaMnO}_3$  to  $67.9 \pm 38.3 \text{ nm}$  for  $\text{La}_{0.77}\text{Te}_{0.23}\text{MnO}_3$  (see online Table S2).

XPS spectra of  $\text{LaMnO}_3$ ,  $\text{La}_{0.9}\text{Te}_{0.10}\text{MnO}_3$ ,  $\text{La}_{0.77}\text{Te}_{0.23}\text{MnO}_3$  are displayed in Fig. 2, showing the La 3d (left), Mn 2p (middle) and Te 3d (right) regions. The characteristic double peak associated with La 3d<sub>5/2</sub> (834.0–834.9 eV) and La 3d<sub>3/2</sub> (851.0–851.9 eV) are observed, with the La 3d<sub>5/2</sub> binding energy consistent with a  $\text{La}^{3+}$  oxidation state.<sup>[7,11,20–22]</sup> The peak at 874 eV, visible for the Te-containing samples has been assigned to the Te Auger MNN. The Te 3d photoemission lines involve the Te 3d<sub>5/2</sub> at 576 eV and Te 3d<sub>3/2</sub> at 586.6 eV. These values are consistent with a  $\text{Te}^{4+}$  oxidation state.<sup>[23,24]</sup> Finally, the photoemission line associated with Mn 2p<sub>3/2</sub> peak centered at 642 eV shows an interesting trend as function of Te content. This line contains contribution from  $\text{Mn}^{2+}$  (640.9 eV) and  $\text{Mn}^{3+}$  (641.9 eV) oxidation state.<sup>[25]</sup> Focusing on this narrow emission range (online Fig. S4), we can see a slight shift of the Mn 2p<sub>3/2</sub> peak towards lower binding energy as the Te content increases. However, given the small differences in binding energies for the two oxidation states, we shall refrain from attempting to estimate  $\text{Mn}^{2+}/\text{Mn}^{3+}$  ratio from these data.

Analysis of the relative composition of La, Te, and Mn, after normalization of the individual photoemission lines by their sensitivity factor and inelastic mean-free path, show a significant A-site surface enrichment. We obtained an A:B ratio of 62:38 for all three materials, broadly in agreement with data reported for other lanthanides.<sup>[7,26]</sup> We have also estimated La:Te ratios of 82:18 and 71:29 for  $\text{La}_{0.90}\text{Te}_{0.10}\text{MnO}_3$  and  $\text{La}_{0.77}\text{Te}_{0.23}\text{MnO}_3$ , respectively. This analysis shows both La and Te substantially segregate to the surface, with a slight increase in Te content with respect to the bulk values.

Figure 3 shows cyclic voltammograms recorded in an argon-saturated 0.1 M KOH solution, revealing a two-step reduction from the initial Mn oxidation state to  $\text{Mn}^{2+}$ .<sup>[7,11,12]</sup> The position of the peak centered at 0.90 V remains almost unaffected, while the second reduction peak is slightly shifted toward higher potentials upon increasing Te content. The most striking difference is in the current densities, with

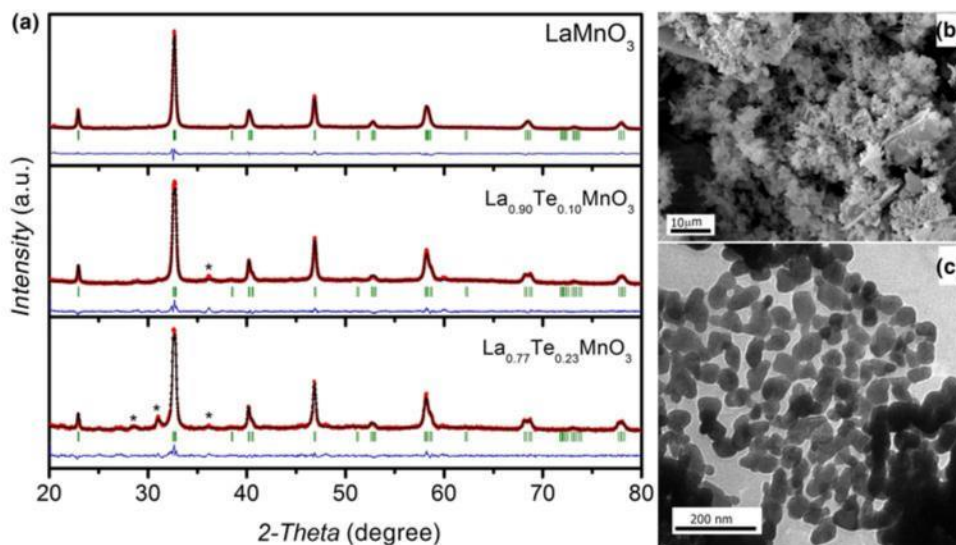


Figure 1. (a) XRD patterns of  $\text{LaMnO}_3$ ,  $\text{La}_{0.90}\text{Te}_{0.10}\text{MnO}_3$ , and  $\text{La}_{0.77}\text{Te}_{0.23}\text{MnO}_3$ . Red dots correspond to the experimental values while the black thin line corresponds to the Rietveld refinement. The thin blue line shows the difference between experimental and refined patterns. The green bars correspond to the positions of the allowed Bragg reflections for the main phase. (b) SEM and (c) TEM images of as-prepared  $\text{LaMnO}_3$ .

both Te-doped materials showing significantly lower responses than  $\text{LaMnO}_3$ . Considering that the catalyst loading is identical (i.e.,  $250 \mu\text{g} \times \text{cm}^{-2}$ ), this behavior indicates a decrease in the number density of electrochemically active Mn-sites at the electrode surface. The faradaic charges associated with the anodic and cathodic peaks are very similar, and the responses remain stable in the studied potential range, suggesting that the stability is not significantly compromised within the timescale of these experiments. Integration of the cathodic current peaks in the range of 0.2–1.2 V enables an estimate of the effective

number density of electroactive Mn sites ( $\Gamma_{\text{Mn}}$ ).<sup>[7]</sup> In order to calculate  $\Gamma_{\text{Mn}}$ , two limiting cases can be assumed with regard to the initial Mn oxidation state: the oxidation state is determined by the mean oxidation state of the A-site taking  $\text{La}^{3+}$  and  $\text{Te}^{4+}$  (case 1), or fixed Mn oxidation state of +3 independently of the A-site composition (case 2). Case 1 implicitly ignores changes in the oxygen content of the oxide, while case 2 assumes that variations in the mean A-site charge is compensated by changes in oxygen stoichiometry. Our previous studies investigating  $\text{La}_{1-x}\text{Ca}_x\text{MnO}_3$ ,<sup>[7]</sup> in which the mean Mn

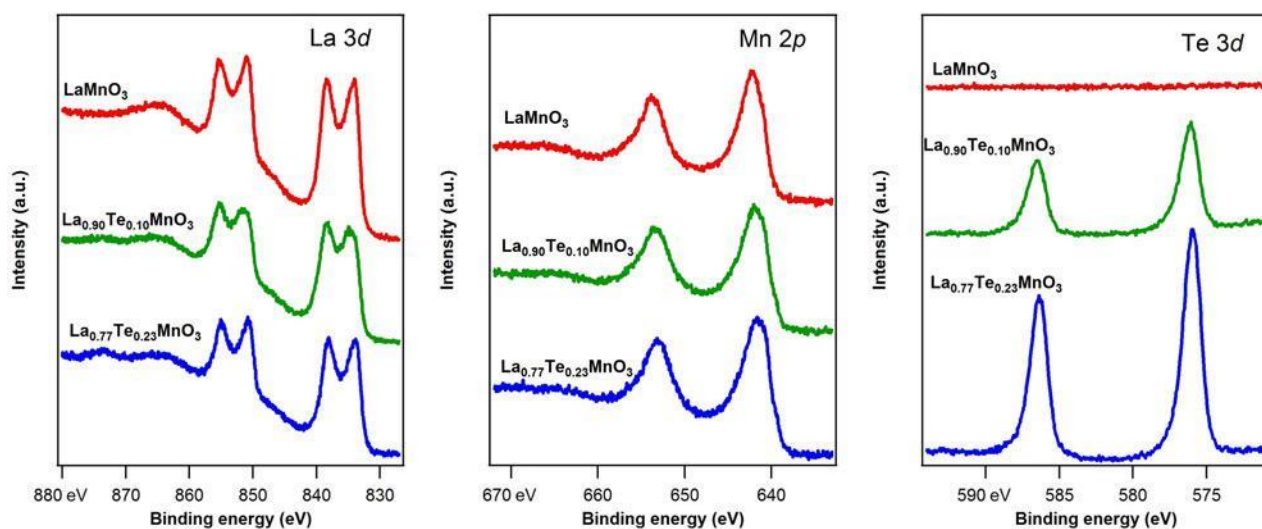


Figure 2. Photoemission spectra of La 3d (left panel), Mn 2p (middle panel) Te 3d (right panel) of the various  $\text{La}_{1-x}\text{Te}_x\text{MnO}_3$  oxides taken in grazing incidence using a monochromatic  $\text{Al K}\alpha$  x-ray source.

Figure 3. Cyclic voltammograms of LaMnO<sub>3</sub>, La<sub>0.90</sub>Te<sub>0.10</sub>MnO<sub>3</sub>, and La<sub>0.77</sub>Te<sub>0.23</sub>MnO<sub>3</sub> supported on Vulcan-carbon in Ar-saturated 0.1 M KOH electrolyte solution at 0.01 V/s. Electrode loaded with 50 μg/cm<sup>2</sup><sub>nation</sub>, 50 μg/cm<sup>2</sup><sub>vulcan</sub>, and 250 μg/cm<sup>2</sup><sub>oxide</sub>.

oxidation state is directly estimated by XANES, confirms case 1 as a valid approximation. In any case, online Table S3 shows that both limiting cases provide values within the same order of magnitude.

The data in online Table S3 show the  $\Gamma_{\text{Mn}}$  is 40%–60% smaller in the Te-doped samples. In view of the similar extent of A-site surface segregation, the smaller  $\Gamma_{\text{Mn}}$  values in the case of the Te containing particles is mainly linked to the smaller specific surface area. Although the mean particle size increases with increasing Te content, we see statistically similar  $\Gamma_{\text{Mn}}$  in both Te containing oxides. This is due to the fact that size dispersion also increases in substantial fashion as shown in online Fig. S3. It should also be mentioned that  $\Gamma_{\text{Mn}}$  in LaMnO<sub>3</sub> prepared at 850 °C (this report) is lower than those prepared at 700 °C from the same ionic liquid precursor,<sup>[7,11]</sup> confirming that calcination temperature is an important parameter to determine A-site segregation.

Figure 4 compares the current measured at the disk ( $i_{\text{DISK}}$ , bottom panel) and the ring ( $i_{\text{RING}}$ , top panel) of carbon-supported LaMnO<sub>3</sub>, La<sub>0.90</sub>Te<sub>0.10</sub>MnO<sub>3</sub>, and La<sub>0.77</sub>Te<sub>0.23</sub>MnO<sub>3</sub> electrodes at 1600 rpm in O<sub>2</sub>-saturated 0.1 M KOH solution. The responses obtained from the Vulcan carbon support under the same experimental conditions are shown in online Fig. S5. All of the catalysts show significantly larger currents than the carbon support, while the ORR onset potential is over 100 mV more positive. LaMnO<sub>3</sub> exhibit larger cathodic current at the disk, with smaller ring current across the potential range. Current-potential curves recorded for La<sub>0.77</sub>Te<sub>0.23</sub>MnO<sub>3</sub> particles at various angular rotation rates are displayed in online Fig. S6. Both Te-doped oxides exhibit rather similar current-potential characteristics.

Figure 5 illustrates the dependence of  $i_{\text{DISK}}$  with the inverse of the angular rotation rate in the case of LaMnO<sub>3</sub> [Fig. 5(a)]

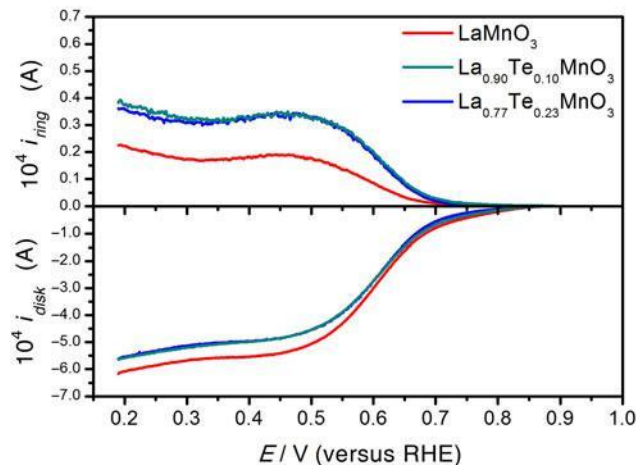


Figure 4. RRDE responses of the various La<sub>x</sub>Te<sub>1-x</sub>MnO<sub>3</sub> nanoparticles supported at Vulcan layer at 1600 rpm in O<sub>2</sub>-saturated 0.1 M KOH at 0.010 V/s. The Pt ring was held at a constant potential of 1.10 V. The oxide content in each electrode was 250 μg/cm<sup>2</sup>.

and La<sub>0.77</sub>Te<sub>0.23</sub>MnO<sub>3</sub> [Fig. 5(b)], which follows the Koutecky–Levich relationship:

$$\frac{1}{i_{\text{DISK}}} = \frac{1}{i_k} + \frac{1}{i_L} = \frac{1}{i_k} + \frac{1}{0.62nAFcD^{2/3}\omega^{-1/6}\nu^{1/2}}, \quad (1)$$

where  $n$  is the number of transferred electrons,  $A$  is the disk geometric area,  $F$  is the Faraday constant,  $c$  is the bulk oxygen concentration ( $1.2 \times 10^{-6}$  mol/cm<sup>3</sup>),<sup>[27]</sup>  $D$  is the oxygen diffusion coefficient ( $1.9 \times 10^{-5}$  cm<sup>2</sup>/s),  $\nu$  is the kinematic viscosity (0.01 cm<sup>2</sup>/s), and  $\omega$  is the angular rotation of the electrode.  $i_k$  and  $i_L$  are the kinetically and mass-transport limiting currents, respectively. It can be observed that LaMnO<sub>3</sub> [Fig. 5(a)] shows a linear dependence, with a slope consistent with  $n = 4$ .<sup>[7,11]</sup> In the case of La<sub>0.77</sub>Te<sub>0.23</sub>MnO<sub>3</sub> [Fig. 5(b)], only a slight deviation from  $n = 4$  is observed at high rotation rate.

The HO<sub>2</sub><sup>-</sup> yield (two-electron process) as a function of potential was calculated from the ring and the disk current values at 1600 rpm [online Fig. S7(a)]. The Vulcan support shows almost 100% HO<sub>2</sub><sup>-</sup> yield between 0.2 and 0.6 V, while LaMnO<sub>3</sub> and both Te-doped catalysts exhibit <30%. The pathway selectivity can also be described in terms of the effective number of electrons shown in online Fig. S7(b). The Vulcan support yields values close to 2, increasing to values above 3.4 upon introduction of the oxide catalysts.

These findings suggest that LaMnO<sub>3</sub> exhibits better performance than the Te-doped under the specific catalyst formulation used, i.e., at equivalent mass loading. However, it should also be considered that mean particle sizes and size dispersion are composition dependent, which have an effect on the overall catalysts performance. Furthermore, XPS data shows an increase in the A-site segregation in the presence of Te, although the surface composition remains dominated by La<sup>3+</sup>.

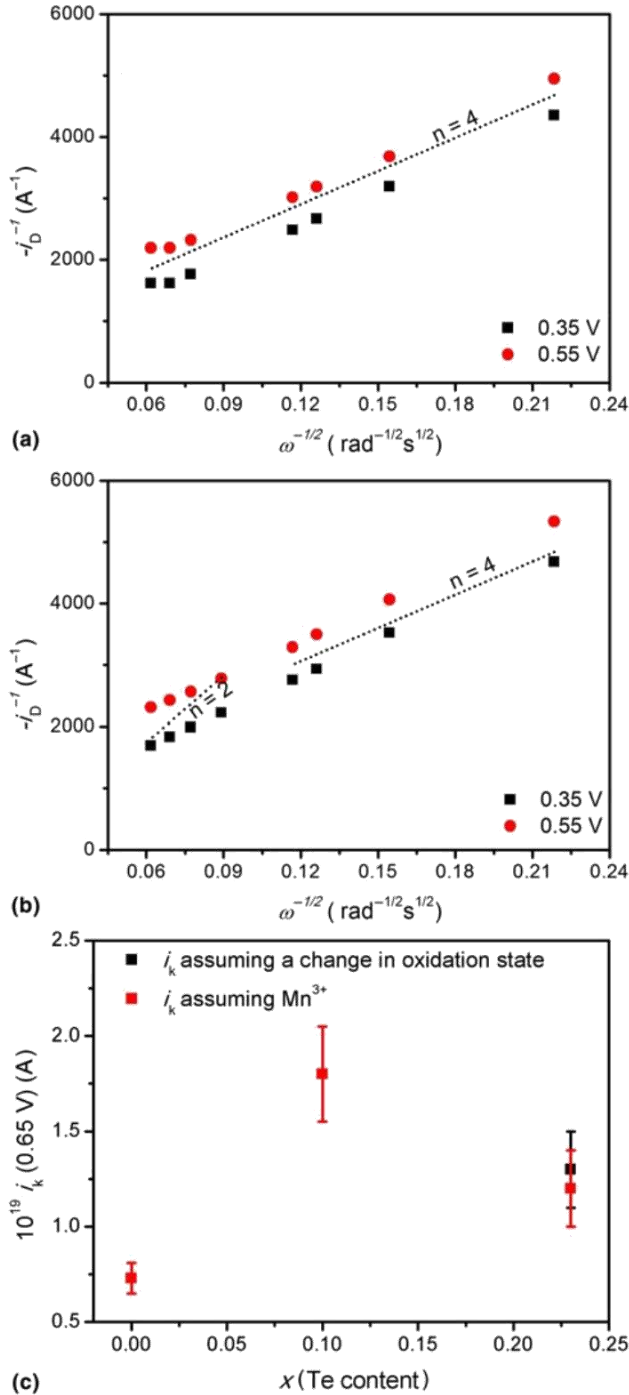


Figure 5. Koutecky–Levich plots of (a) LaMnO<sub>3</sub> and (b) La<sub>0.77</sub>Te<sub>0.23</sub>MnO<sub>3</sub> electrodes in O<sub>2</sub>-saturated 0.1 M KOH at 0.55 and 0.35 V. Dotted lines represent the limiting slopes for the two and four-electron processes. (c) Kinetically limited current at 0.65 V normalized by the effective number of electroactive Mn atoms ( $\hat{i}_k$ ).

In order to account for these parameters, the kinetically limiting current can be normalized by  $\Gamma_{\text{Mn}}$ , i.e.,  $\hat{i}_k = i_k / (A \times \Gamma_{\text{Mn}})$ .<sup>[7]</sup>

Figure 5(c) illustrates the variation of  $\hat{i}_k$  at 0.65 V as a function of the Te content, obtained from at least three different

samples from various synthesis batches. The contribution of the carbon support to the overall current at this potential is negligible in comparison with the oxide loaded catalysts (see online Fig. S4). Two sets of data are plotted based on the two limiting cases used for calculating  $\Gamma_{\text{Mn}}$ . It is interesting to see the performance of electrochemically active surface Mn sites increases on average in the presence of Te. Surface Mn sites in materials containing 10% Te appears twice more active than surface Mn-sites in LaMnO<sub>3</sub>. The performance seems to slightly degrade for larger Te content.

We rationalize this early trend in terms of changes in the electron density at Mn sites. Incorporating 10% Te in the A-site, most probably in a 4+ oxidation state, effectively increases the electron density at the B-site, leading to an enhancement in the catalytic activity for ORR. Indeed, the slight shift in the binding energy of the Mn 2p<sub>3/2</sub> peak suggests a decrease in the oxidation state on Mn sites in the presence of Te (Figs 2 and S4). A similar correlation have been recently reported in the case La<sub>1-x</sub>Ca<sub>x</sub>MnO<sub>3</sub>.<sup>[7]</sup>

In conclusion, these studies reveal an increase in the mean activity of surface Mn sites upon Te<sup>4+</sup> doping in the A-site. The most active surface Mn sites were obtained upon 10% replacement of La<sup>3+</sup> by Te<sup>4+</sup>, leading to an increase of the electron density at the Mn site without compromising the coordination structure. To confirm this hypothesis, a number of parameters should be systematically explored such as the effect of low oxidation state cations with different sizes as well as the activity of different LaMnO<sub>3</sub> phases. In any case, our studies demonstrate the need of establishing universal descriptors, such as  $\hat{i}_k$ , which uncovers the mean activity of surface Mn sites, independently of the particle size, dispersion quality, and complex phenomena such as A-site segregation.

## Acknowledgment

The authors acknowledge Dr. Devendra Tiwari and Gael Gobaille-Shaw for the fruitful discussions. V. C. and D. J. F. are thankful to the UK Catalysis Hub (EPSRC grants EP/K014706/1 and EP/K014714/1) for resources and support. L. J. M. and D. J. F. are also grateful to the EPSRC Centre for Doctoral Training in Catalysis for the financial support. SEM/EDX and TEM studies were carried out in the Chemistry Imaging Facility at the University of Bristol with equipment partly funded by EPSRC (EP/K035746/1 and EP/M028216/1). Authors acknowledge access to the Bristol NanoESCA Facility under EPSRC Strategic Equipment Grant EP/M000605/1. D. J. F. also acknowledges the University Research Fellowship (2015–2016) provided by the Institute of Advanced Studies of the University of Bristol.

## References

1. F. Cheng and J. Chen: Metal-air batteries: from oxygen reduction electrochemistry to cathode catalysts. *Chem. Soc. Rev.* 41, 2172 (2012).
2. D.U. Lee, P. Xu, Z.P. Cano, A.G. Kashkooli, M.G. Park, and Z. Chen: Recent progress and perspectives on bi-functional oxygen electrocatalysts for advanced rechargeable metal-air batteries. *J. Mater. Chem. A* 4, 7107 (2016).
3. L. Li, X. Feng, S. Chen, F. Shi, K. Xiong, W. Ding, X. Qi, J. Hu, Z. Wei, L.-J. Wan, and M. Xia: Insight into the effect of oxygen vacancy concentration on the catalytic performance of MnO<sub>2</sub>. *ACS Catal.* 5, 4825 (2015).
4. W.G. Hardin, J.T. Mefford, D.A. Slanac, B.B. Patel, X. Wang, S. Dai, X. Zhao, R.S. Ruoff, K.P. Johnston, and K.J. Stevenson: Tuning the electrocatalytic activity of perovskites through active site variation and support interactions. *Chem. Mater.* 26, 3368 (2014).
5. J. Suntivich, H.A. Gasteiger, N. Yabuuchi, H. Nakanishi, J. B. Goodenough, and Y. Shao-Horn: Design principles for oxygen-reduction activity on perovskite oxide catalysts for fuel cells and metal-air batteries. *Nat. Chem.* 3, 546 (2011).
6. K.A. Stoerzinger, M. Risch, B. Han, and Y. Shao-Horn: Recent insights into manganese oxides in catalyzing oxygen reduction kinetics. *ACS Catal.* 5, 6021 (2015).
7. V. Celorrio, L. Calvillo, E. Dann, G. Granozzi, A. Aguadero, D. Kramer, A. E. Russell, and D.J. Fermin: Oxygen reduction reaction at La<sub>x</sub>Ca<sub>1-x</sub>MnO<sub>3</sub> nanostructures: interplay between A-site segregation and B-site valency. *Catal. Sci. Tech.* 6, 7231 (2016).
8. X. Ge, A. Sumboja, D. Wu, T. An, B. Li, F.W.T. Goh, T.S.A. Hor, Y. Zong, and Z. Liu: Oxygen reduction in alkaline media: from mechanisms to recent advances of catalysts. *ACS Catal.* 5, 4643 (2015).
9. F. Calle-Vallejo, N.G. Inoglu, H.-Y. Su, J.I. Martinez, I.C. Man, M.T. M. Koper, J.R. Kitchin, and J. Rossmeisl: Number of outer electrons as descriptor for adsorption processes on transition metals and their oxides. *Chem. Sci.* 4, 1245 (2013).
10. W. Lee, J.W. Han, Y. Chen, Z. Cai, and B. Yildiz: Cation size mismatch and charge interactions drive dopant segregation at the surfaces of manganite perovskites. *J. Am. Chem. Soc.* 135, 7909 (2013).
11. V. Celorrio, E. Dann, L. Calvillo, D.J. Morgan, S.R. Hall, and D.J. Fermin: Oxygen reduction at carbon-supported lanthanides: the role of the B-site. *ChemElectroChem* 3, 283 (2016).
12. A.S. Ryabova, F.S. Napol'skiy, T. Poux, S.Y. Istomin, A. Bonnefont, D.M. Antipin, A.Y. Baranchikov, E.E. Levin, A.M. Abakumov, G. Kéranguéven, E.V. Antipov, G.A. Tsirlina, and E.R. Savinova: Rationalizing the influence of the Mn(IV)/Mn(III) red-ox transition on the electrocatalytic activity of manganese oxides in the oxygen reduction reaction. *Electrochim. Acta* 187, 161 (2016).
13. W.T. Hong, M. Risch, K.A. Stoerzinger, A. Grimaud, J. Suntivich, and Y. Shao-Horn: Toward the rational design of non-precious transition metal oxides for oxygen electrocatalysis. *Energy Environ. Sci.* 8, 1404 (2015).
14. J. Yang, W.H. Song, Y.Q. Ma, R.L. Zhang, and Y.P. Sun: Determination of oxygen stoichiometry in the mixed-valent manganites. *J. Magn. Magn. Mater.* 285, 417 (2005).
15. D.C. Green, S. Glatzel, A.M. Collins, A.J. Patil, and S.R. Hall: A new general synthetic strategy for phase-pure complex functional materials. *Adv. Mater.* 24, 5767 (2012).
16. J. Rodríguez-Carvajal: Recent advances in magnetic structure determination by neutron powder diffraction. *Phys. B: Condens. Matter* 192, 55 (1993).
17. H. Rietveld: A profile refinement method for nuclear and magnetic structures. *J. Appl. Crystallogr.* 2, 65 (1969).
18. J. Yang, W.H. Song, Y.Q. Ma, R.L. Zhang, B.C. Zhao, Z.G. Sheng, G.H. Zheng, J.M. Dai, and Y.P. Sun: Insulator-metal transition and the magnetic phase diagram of La<sub>1-x</sub>TexMnO<sub>3</sub> (0.1 ≤ x ≤ 0.6). *Mater. Chem. Phys.* 94, 62 (2005).
19. G.H. Zheng, Y.P. Sun, X.B. Zhu, and W.H. Song: Transport, magnetic, internal friction, and Young's modulus in the Y-doped manganites La<sub>0.9-x</sub>Y<sub>x</sub>Te<sub>0.1</sub>MnO<sub>3</sub>. *J. Solid State Chem.* 179, 1394 (2006).
20. M.F. Sunding, K. Hadidi, S. Diplas, O.M. Løvvik, T.E. Norby, and A. E. Gunnæs: XPS characterisation of in situ treated lanthanum oxide and hydroxide using tailored charge referencing and peak fitting procedures. *J. Electron. Spectrosc. Relat. Phenom.* 184, 399 (2011).
21. M.C. Álvarez-Galván, V.A. de la Peña O'Shea, G. Arzamendi, B. Pawelec, L. M. Gandía, and J.L.G. Fierro: Methyl ethyl ketone combustion over La-transition metal (Cr, Co, Ni, Mn) perovskites. *Appl. Catal. B* 92, 445 (2009).
22. K. Bolwin, W. Schnurnberger, and G. Schiller: Influence of valence band states on the core hole screening in lanthanide perovskite compounds. *Z. Phys. B* 72, 203 (1988).
23. A.B. Christie, I. Sutherland, and J.M. Walls: Studies of the composition, ion-induced reduction and preferential sputtering of anodic oxide films on Hg<sub>0.8</sub>Cd<sub>0.2</sub>Te by XPS. *Surf. Sci.* 135, 225 (1983).
24. R.F.C. Farrow, P.N.J. Dennis, H.E. Bishop, N.R. Smart, and J.T. M. Wotherspoon: The composition of anodic oxide films on Hg<sub>0.8</sub>Cd<sub>0.2</sub>Te. *Thin Solid Films* 88, 87 (1982).
25. V. Di Castro and G. Polzonetti: XPS study of MnO oxidation. *J. Electron. Spectrosc. Relat. Phenom.* 48, 117 (1989).
26. J. Druce, H. Tellez, M. Burriel, M.D. Sharp, L.J. Fawcett, S.N. Cook, D. S. McPhail, T. Ishihara, H.H. Brongersma, and J.A. Kilner: Surface termination and subsurface restructuring of perovskite-based solid oxide electrode materials. *Energy Environ. Sci.* 7, 3593 (2014).
27. A.J. Bard: Chapter 9: Methods involving forced convection-hydrodynamic methods. In *Electrochemical Methods: Fundamentals and Applications*, edited by A.J. Bard and L.R. Faulkner (Wiley, New York, 1980), pp. 331–367.